Spin waves in alloys at finite temperatures: Application to the FeCo magnonic crystal

Sebastian Paischer,[1,*] Paweł A. Buczek,[2] Nadine Buczek,[3] David Eilmsteiner,[1] and Arthur Ernst[4,1]

[1]*Institute for Theoretical Physics, Johannes Kepler University Linz, Altenberger Straße 69, 4040 Linz, Austria*

[2]*Department of Engineering and Computer Sciences, Hamburg University of Applied Sciences, Berliner Tor 7, 20099 Hamburg, Germany*

[3]*Department of Applied Natural Sciences, Lübeck University of Applied Sciences, Mönkhofer Weg 239, 23562 Lübeck, Germany*

[4]*Max-Planck-Institut of Microstructure Physics, Weinberg 2, 06120 Halle (Saale), Germany*

(Received 23 November 2020; revised 30 April 2021; accepted 14 June 2021; published 2 July 2021)

We study theoretically the influence of temperature and disorder on the spin-wave spectrum of the magnonic crystal $Fe_{1-c}Co_c$. Our formalism is based on the analysis of a Heisenberg Hamiltonian by means of the wave vector and frequency-dependent transverse magnetic susceptibility. The exchange integrals entering the model are obtained from the *ab initio* magnetic force theorem. The coherent potential approximation is employed to treat the disorder and random phase approximation in order to account for the softening of the magnon spectrum at finite temperatures. The alloy turns out to exhibit many advantageous properties for spintronic applications. Apart from a high Curie temperature, its magnonic band gap remains stable at elevated temperatures and is largely unaffected by the disorder. We pay particular attention to the attenuation of magnons introduced by the alloying. The damping turns out to be a nonmonotonic function of the impurity concentration due to the nontrivial evolution of the value of exchange integrals with the Co concentration. The disorder-induced damping of magnons is estimated to be much smaller than their Landau damping.

DOI: 10.1103/PhysRevB.104.024403

I. INTRODUCTION

Magnon spintronics, or magnonics, is a novel promising strategy in the engineering of data processors [1]. It takes advantage of spin waves (also called magnons) in order to perform logical computations [2,3]. Magnons emerge as collective excitations of magnetically ordered solids and can be pictured as a wavelike coherent precession of atomic moments [4]. In periodic structures, including atomic lattices, these quasiparticles are Bloch waves, carrying energy and crystal momentum. Magnonic computers avoid numerous drawbacks of classical semiconductor-based computers, but they rely heavily on suitably designed magnon propagation media. Their particularly relevant class are *magnonic crystals* [5,6] featuring spin-wave propagation properties not typically found in common magnetic solids such as elemental ferro- and antiferromagnets, especially the emergence of a *magnonic gap*, i.e., frequency bands in which magnon states cannot propagate in the solid [7,8]. This feature, combined with a unique spin-wave dispersion close to the band edges, provides a rich toolbox for magnon mode engineering, including the possibility of selective spin-wave excitations and propagation, magnon mode confinement and deceleration, and band-gap soliton generation [9–11].

The bulk of the current research in this domain revolves around the utilization of long-wavelength magnons with energies in the gigahertz band. Nevertheless, in order to definitely push the size and speed limits of modern semiconductor computers, one must resort to the spin waves in the terahertz regime. While the foundations are laid for magnonic information processing in the terahertz regime, the potential for terahertz magnonics remains vastly unexplored [12]. At the same time, one expects well-defined spin waves in this energy range [13], and in systems with many different atoms in the primitive cell, the modes may well arrange in bands separated by a magnonic gap [14], yielding natural magnonic crystals.

Here, we concentrate on the ferromagnetic $Fe_{1-c}Co_c$ alloy. With typical magnon energies well within the terahertz range, a high Curie temperature [15,16], and the band gap in the spectrum, opening due to the large difference in the interaction strengths and magnetic moments of the constituents and remaining stable at elevated temperatures, the alloy family shows all the necessary properties for terahertz magnonic crystals. It is interesting to note that the magnonic crystals used in terahertz applications are typically artificial heterostructures obtained from elaborate fabrication processes. On the contrary, in the terahertz range, the natural microscopic arrangement of atoms in alloys such as $Fe_{1-c}Co_c$ would suffice to create cheap magnonic crystals.

In metals, the lifetime of the modes is limited by the interaction of these collective modes with the single-particle continuum, called Landau damping [17–19], but means of the viable engineering of long-living magnons has been proposed, such as reducing the system's dimensionality and alloying [20]. The latter method leads to a further momentum dissipation mechanism, in which the Bloch waves cease to be the eigenstates of the magnetic Heisenberg-like Hamiltonian and acquire a finite lifetime arising from the scattering on the crystal imperfections [21,22]. This picture of the weak attenuation might break down if the magnon spectra become dominated by strongly spatially localized modes. A further

*sebastian.paischer@jku.at

mechanism limiting the lifetime of the magnon modes, and thus their potential to propagate dissipationlessly through the medium, is the interaction of the modes with a thermal bath.

Solids, and in particular nanostructures, often feature structural imperfections. Furthermore, in order to be usable, the magnonic computers must be able to operate at and typically well above room temperature. Thus, it is prudent to delve into the central question of this paper, namely how the magnonic properties evolve in real, imperfect, or alloyed solids at nonzero temperatures. We show that the increase of the disorder in the $Fe_{1-c}Co_c$ alloy not only preserves the magnonic gap but can even be used to precisely engineer its value and further properties.

Among others, we address the influence of temperature and disorder on the magnonic band gap as well as on the dispersion and lifetimes of the spin waves. Our formalism is based on the coherent potential approximation (CPA) applied to the disordered Heisenberg ferromagnet [21]. This description of magnetic degrees of freedom with an effective Heisenberg Hamiltonian, although originally put forth for the description of magnetic insulators, has been shown to yield remarkably accurate results for metallic magnets also beyond the long-wavelength limit in which it can be shown to be formally accurate [23–26]. The superiority of our method compared to other treatments of the same problem is the possibility to account for complex crystal structures. To incorporate finite-temperature effects, we implemented a modified version of the random phase approximation (RPA) discussed in Ref. [27]. Our formalism does not include the Landau damping of the spin waves. This attenuation mechanism can be pronounced in metallic magnonic crystals and can be described within the framework of many-body perturbation theory (MBT) [28,29] or time-dependent density functional theory (TDDFT) [18] (called "dynamical methods"). Unfortunately, at the moment, no feasible formal and computational methodology allowing one to incorporate the effects of disorder into these two approaches has been put forward. However, those dynamical methods reveal that in most ordered three-dimensional $3d$ itinerant magnets, except for moderate Landau broadening, well-defined magnons are indeed expected in the entire Brillouin zone, possibly with the exception of bcc Fe where the "spin-wave disappearance" phenomenon sets in in limited parts of the Brillouin zone [18]. Relevant for the case of FeCo, the MBT calculations of Şaşıoğlu *et al.* [28] predict the existence of well-defined spin waves in the entire zone both for the acoustic and optical modes. Correspondingly, neutron scattering experiments (cf. references in Ref. [18]) and spin-polarized electron energy loss spectroscopy [30–33] probe clear high-energy spin-wave signals in the entire zone. Although neither calculations based on the magnetic force theorem (MFT) nor TDDFT can properly describe spin waves in Ni, magnons in Co and Fe are well reproduced for almost the whole Brillouin zone (BZ) and a large frequency range (see, e.g., Refs. [32,33]). An even better agreement between the MFT calculations and experiment is achieved in layered materials [34–39], caused by a significantly weaker interaction with the Stoner continuum compared to 3D materials. When the associated Heisenberg model is employed at elevated temperatures it yields a very good account of the phase transition temperatures (even in bcc Fe), indicating that the high-temperature phase is essentially correctly captured as well [40,41]. Thus it is reasonable to apply the Heisenberg model to study the impact of disorder on the damping of spin waves.

The paper is organized as follows: In Sec. II, the theoretical background of the RPA-CPA theory for disordered Heisenberg ferromagnets is discussed. Some numerical details are given in Sec. III. The results are presented in Sec. IV.

II. THEORY

The Heisenberg ferromagnet is characterized by the Hamiltonian

$$H = -\frac{1}{2}\sum_{i,j} J_{ij}\, \boldsymbol{e}_i \cdot \boldsymbol{e}_j, \tag{1}$$

where J_{ij} are the exchange parameters which can be obtained from the magnetic force theorem [42,43] and $\boldsymbol{e}_i$ is a unit vector in the direction of the magnetic moment. To calculate the magnon properties, the transverse susceptibility [44]

$$\chi_{ij}(t,t') = -i\,\Theta(t-t')\overline{[\mu_i^+(t), \mu_j^-(t')]}, \tag{2}$$

with $\mu_i^{\pm} = \mu_i^x \pm i\mu_i^y$, μ_i^{α} being the α component of the magnetic moment $\boldsymbol{\mu}_i$ on the lattice site i, and the overline represents a thermal average, is computed. The corresponding equation of motion reads

$$\begin{aligned} z\chi_{ij}(z) = {} & 2g\delta_{ij}\,\overline{\mu_i^z} - g\sum_{\ell}\frac{\overline{\mu_i^z}}{\mu_i\mu_\ell} J_{i\ell}\,\chi_{\ell j}(z) \\ & + g\sum_{\ell}\frac{\overline{\mu_\ell^z}}{\mu_i\mu_\ell} J_{i\ell}\,\chi_{ij}(z). \end{aligned} \tag{3}$$

with the electron Landé factor g and the energy $z = E + i\varepsilon$. The disorder is modeled by defining the occupation variables

$$p^{i\alpha}(\boldsymbol{R}) = \begin{cases} 1 & \text{species } \alpha \text{ on basis site } i \text{ in unit cell } \boldsymbol{R}, \\ 0 & \text{else}, \end{cases} \tag{4}$$

and a species resolved Fourier transformation of the susceptibility,

$$\chi_{ij}^{\alpha\beta}(\boldsymbol{k},\boldsymbol{k}') := \sum_{\boldsymbol{R},\boldsymbol{R}'} p^{i\alpha}(\boldsymbol{R}) e^{-i\boldsymbol{k}\cdot\boldsymbol{R}}\,\chi_{ij}(\boldsymbol{R},\boldsymbol{R}')\,p^{j\beta}(\boldsymbol{R}')e^{i\boldsymbol{k}'\cdot\boldsymbol{R}'}. \tag{5}$$

In the following, it is useful to introduce a combined site and species index denoted by $(i) = i\alpha$, $(j) = j\beta$, etc. Writing the susceptibility given in formula (3) as a series and performing the Fourier transformation [Eq. (5)] leads to expressions with products of Fourier transformed occupation variables

$$\varrho^{(i)}(\boldsymbol{k}) = \sum_{\boldsymbol{R}} p^{(i)}(\boldsymbol{R}) e^{-i\boldsymbol{k}\cdot\boldsymbol{R}}. \tag{6}$$

The averaging process needs to be done very carefully as described in Refs. [21,45] and leads to the appearance of cumulants of order n given by

$$\begin{aligned} \mathcal{C}^n_{(\ell_1)(\ell_2)\cdots(\ell_n)}(\boldsymbol{k}_1, \boldsymbol{k}_2 \cdots \boldsymbol{k}_n) = {} & \mathcal{P}^n_{(\ell_1)(\ell_2)\cdots(\ell_n)}(\boldsymbol{c}) \\ & \cdot \Omega_{\mathrm{BZ}}\,\delta(\boldsymbol{k}_1 + \boldsymbol{k}_2 + \cdots + \boldsymbol{k}_n), \end{aligned} \tag{7}$$

where $\boldsymbol{c}$ is a matrix with the concentrations of each species on the sublattices and the weight functions $\mathcal{P}^n_{(\ell_1)(\ell_2)\cdots(\ell_n)}(\boldsymbol{c})$. There

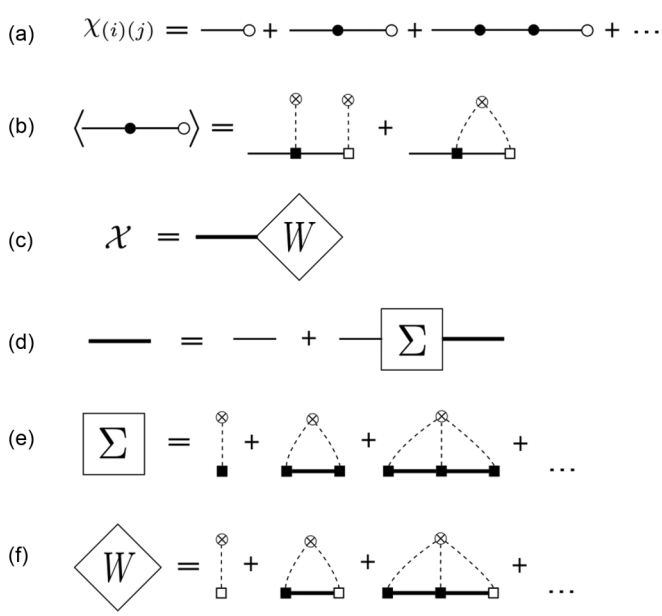

FIG. 1. Diagrammatic representation of the main results of the CPA theory. (a) Fourier transformation of series (3), (b) average of the second term in (a), (c) the averaged susceptibility $\mathcal{X}$ written as a product of the effective medium propagator Ξ (thick line) and the spin weight W, (d) Dyson equation for the effective medium propagator, (e) definition of the self-energy Σ, and (f) definition of the spin weight W.

is no analytic representation of the latter but the first two are given by

$$\mathcal{P}^1_{(i)} = c^{(i)},$$
$$\mathcal{P}^2_{(i)(j)} = \delta_{ij}(\delta_{\alpha\beta}\, c^{(i)} - c^{(i)}\, c^{(j)}). \tag{8}$$

A summary of the resulting formulas after the Fourier transformation and the averaging can be found in Fig. 1 in diagrammatic form where the following symbols have been used:

(1) The τ matrix

$$\tau^{(\ell)}_{(i)(j)}(\boldsymbol{k},\boldsymbol{k}') = g\mu^{-1}_{(j)}\Big(J_{(j)(\ell)}(\boldsymbol{k}-\boldsymbol{k}')\frac{\overline{\mu}^z_{(\ell)}}{\mu_{(\ell)}}\delta_{(i)(j)} - J_{(\ell)(j)}(\boldsymbol{k}')\frac{\overline{\mu}^z_{(i)}}{\mu_{(i)}}\delta_{(i)(\ell)}\Big), \tag{9}$$

where

$$J_{(i)(j)}(\boldsymbol{k}) = \sum_{\boldsymbol{R}} J_{(i)(j)}(\boldsymbol{R})e^{-i\boldsymbol{k}\cdot\boldsymbol{R}}, \tag{10}$$

is represented by a solid square.

(2) The solid circle represents a T matrix,

$$T_{(i)(j)}(\boldsymbol{k},\boldsymbol{k}') = \sum_{(\ell)} \varrho^{(\ell)}(\boldsymbol{k}-\boldsymbol{k}')\tau^{(\ell)}_{(i)(j)}(\boldsymbol{k},\boldsymbol{k}'). \tag{11}$$

(3) An open square stands for an σ matrix,

$$\sigma^{(\ell)}_{(i)(j)} = 2g\delta_{(i)(j)}\delta_{(i)(\ell)}\overline{\mu}^z_{(\ell)}. \tag{12}$$

(4) The S matrix is depicted as an open circle and is given by

$$S_{(i)(j)}(\boldsymbol{k},\boldsymbol{k}') = \sum_{(\ell)} \varrho^{(\ell)}(\boldsymbol{k}-\boldsymbol{k}')\sigma^{(\ell)}_{(i)(j)}. \tag{13}$$

(5) The propagator of uncoupled magnetic moments, represented by a solid line, is given as

$$\Gamma_{(i)(j)}(z) = z^{-1}\delta_{(i)(j)}. \tag{14}$$

(6) A cumulant of order n is represented by a crossed circle, where the order is given by the number of dashed lines ending at it.

Furthermore, two rules for the interpretation of the diagrams need to be followed:

(1) The elements brought together in a diagram undergo a matrix multiplication in the $(i)(j)$ space. The corresponding matrix indices are written as subscripts in the definitions above.

(2) Every internal free propagator is assigned a momentum which is integrated over,

$$\frac{1}{\Omega_{\mathrm{BZ}}}\int_{\Omega_{\mathrm{BZ}}} d^3k_1. \tag{15}$$

Every term of the series for the susceptibility in Fig. 1(a) is averaged independently. The result for the second term is shown in Fig. 1(b). In the CPA, crossed terms, which appear in the fourth- and higher-order terms, are neglected. This model represents a single-site approximation and neglects all correlations between two or more sites. As these averaged diagrams consist of two different vertices (solid and open squares), the averaged susceptibility can be written as a product of two different contributions which we call the effective medium propagator Ξ and the spin weight W as is shown in Fig. 1(c). The effective medium propagator is given in terms of a Dyson equation shown in Fig. 1(d) with a self-energy defined in Fig. 1(e). Together with the definition of the spin weight in Fig. 1(f), all noncrossed diagrams of the averaged susceptibility can be constructed.

The calculation of the self-energy is done through the partial self-energies defined by

$$c^{i\alpha}\hat{\boldsymbol{\Sigma}}^{i\alpha} = \mathcal{P}^1_{i\alpha}\mathbb{1} + \mathcal{P}^2_{i\beta,i\alpha}\boldsymbol{M}^{i\beta} + \mathcal{P}^3_{i\gamma,i\beta,i\alpha}\boldsymbol{M}^{i\gamma}\boldsymbol{M}^{i\beta} + \cdots, \tag{16}$$

where the M matrix is given by

$$\boldsymbol{M}^{(i)}(z,\boldsymbol{k},\boldsymbol{k}') = \boldsymbol{\tau}^{(i)}(\boldsymbol{k},\boldsymbol{k}')\boldsymbol{\Xi}(z,\boldsymbol{k}'). \tag{17}$$

With that the self-energy is given by

$$\boldsymbol{\Sigma}(z,\boldsymbol{R},\boldsymbol{R}') = \sum_{(i)} c^{(i)} \sum_{\boldsymbol{R}_1} \hat{\boldsymbol{\Sigma}}^{(i)}(z,\boldsymbol{R},\boldsymbol{R}_1)\boldsymbol{\tau}^{(i)}(\boldsymbol{R}_1,\boldsymbol{R}'), \tag{18}$$

which can also be seen through its diagrammatic definition. The self-consistency equation inspired by the works of Refs. [45,46] is given by

$$\hat{\boldsymbol{\Sigma}}^{(i)} = [\mathbb{1} - (\boldsymbol{M}^{(i)} - \bar{\boldsymbol{\Sigma}}^i)]^{-1}, \tag{19}$$

where the helping quantity

$$\bar{\boldsymbol{\Sigma}}^i(\boldsymbol{R},\boldsymbol{R}') = \sum_{\alpha\in I_i}\sum_{\boldsymbol{R}_1} c_{i\alpha}\hat{\boldsymbol{\Sigma}}^{i\alpha}(\boldsymbol{R},\boldsymbol{R}_1)\boldsymbol{M}^{i\alpha}(\boldsymbol{R}_1,\boldsymbol{R}') \tag{20}$$

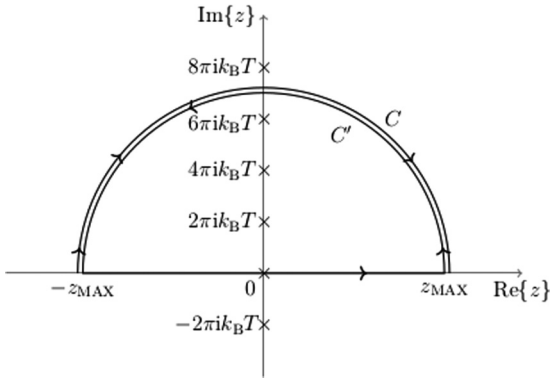

FIG. 2. Integration contour used to calculate $\Phi_{(i)}$. The crosses on the imaginary axis mark the poles of $\frac{1}{e^{\beta z}-1}$.

is used. Equation (19) is used to calculate a new self-energy from the effective medium propagator with which through Fig. 1(c) a new effective medium propagator can be calculated.

The temperature dependence is calculated through the average magnon number

$$\Phi_{(i)} = \mathrm{Im}\int_{-\infty}^{\infty} dz \frac{D_{(i)}(z)}{e^{\frac{z}{k_B T}} - 1}, \tag{21}$$

where

$$D_{(i)}(z) = -\frac{1}{\pi}\int_{\Omega_{BZ}} d^3k \frac{\mathcal{X}_{(i)(i)}(z,\boldsymbol{k})}{2gc_{(i)}\overline{\mu}^z_{(i)}}. \tag{22}$$

Note that the imaginary part of this quantity $D_{(i)}(z)$ is the magnonic density of states. Following the theory of Callen [27] and its implementations in simple disordered and complex ordered systems [40,47,48], the thermally averaged z components of the magnetic moments are

$$\overline{\mu}^z_{(i)} = g\frac{\left(\frac{\mu_{(i)}}{g} - \Phi_{(i)}\right)(1+\Phi_{(i)})^{\mu_{(i)}+1} + \left(\frac{\mu_{(i)}}{g} + 1 + \Phi_{(i)}\right)\Phi_{(i)}^{\mu_{(i)}+1}}{(1+\Phi_{(i)})^{\mu_{(i)}+1} - (\Phi_{(i)})^{\mu_{(i)}+1}}. \tag{23}$$

III. IMPLEMENTATION

The integrals in $\boldsymbol{k}$ space [see Eq. (22)] were computed using the tetrahedron method [49]. The energy integral is problematic as $D_{(i)}(z)$ is a rapidly changing function along the real axis and in addition to that the Bose factor $\frac{1}{e^{\frac{z}{k_B T}}-1}$ has a pole at $z = 0$. Therefore, the energy integral was implemented using complex contour integration. The problem was tackled by calculating two complex integrals, which are shown in Fig. 2. C is a semicircle with radius z_{MAX} and C' is a closed contour consisting of the same arc as C but in the opposite direction and a straight line infinitesimally close to the real axis. The closed contour C' was evaluated using the residue theorem as the Bose factor has poles along the imaginary axis at $z_n = 2n\pi i k_B T$ with $n \in \mathbb{Z}$. The values of the residues are given by

$$R(z_n) = k_B T D_{(i)}(z_n). \tag{24}$$

The sum of both contours C and C' gives the integral parallel and infinitesimally close along the real axis. This method is based on the fact that the integrand in Eq. (21) is analytic almost everywhere in the complex upper half plane and on the fact that it vanishes for very large positive and negative energies. The radius of the integration contour z_{MAX} was estimated using the Gershgorin disk theorem [50].

Another complication arises from the fact that the Bose factor has a singularity at $z = 0$. As mentioned above, the method used here gives the integral parallel to the real axis at an infinitesimal distance Δ. Therefore the integral calculated through the complex contour integral described above is

$$\Phi_{(i)} = \mathrm{Im}\int_{-\infty}^{\infty} \frac{D_{(i)}(E + i\Delta)}{e^{\beta E} - 1 + i\Delta\beta e^{\beta E}} dE, \tag{25}$$

where $e^{\Delta x} \approx 1 + \Delta x$ was used. This can be rewritten using the Shokotski-Plemelj theorem

$$\lim_{\Delta\to 0}\frac{1}{x + i\Delta} = \frac{\mathcal{P}}{x} - i\pi\delta(x), \tag{26}$$

where $\mathcal{P}$ is the Cauchy principal value. Now, $\Phi_{(i)}$ is given by the principal value integral but because of the extension of the integration contour, an additional contribution

$$i\pi k_B T D_{(i)}(0) \tag{27}$$

is picked up. This contribution is spurious and needs to be subtracted from the result of the integral.

In the limit $T \to T_C$, the average magnon number $\Phi_{(i)}$ goes to infinity, which allows a series expansion of Eq. (23) in $\frac{1}{\Phi_{(i)}}$:

$$\overline{\mu}^z_{(i)} = \frac{\mu_{(i)}(\mu_{(i)} + g)}{3g\Phi_{(i)}} + O\left[\left(\frac{1}{\Phi_{(i)}}\right)^2\right]. \tag{28}$$

Expanding the exponential in formula (21) and inserting it in the series expansion above leads to

$$\overline{\mu}^z_{(i)} = -\pi\frac{\mu_{(i)}(\mu_{(i)} + g)}{3gk_B T_C}\left[\int dz \int d^3k \frac{\mathcal{X}_{(i)(i)}(z,\boldsymbol{k})}{2gc_{(i)}\overline{\mu}^z_{(i)} z}\right]^{-1}. \tag{29}$$

An important point is that the latter equation still holds if all the averaged magnetic moments are scaled by an arbitrary constant factor. This fact is obvious in ordered systems as is shown in Ref. [40] and also holds in substitutionally disordered systems. Using this property, the calculation of the Curie temperature can be done by treating the averaged moments as a vector and solving the equation

$$\overline{\mu}^z_{(i)} = -\pi\frac{\mu_{(i)}(\mu_{(i)} + g)}{3gk_B}\left[\int dz \int d^3k \frac{\mathcal{X}_{(i)(i)}(z,\boldsymbol{k})}{2gc_{(i)}\overline{\mu}^z_{(i)} z}\right]^{-1} \tag{30}$$

iteratively while also normalizing this vector to an arbitrary length in each step. Note that in Eq. (30) the factor T_C is omitted. After convergence is reached, the Curie temperature is given by the length of the vector.

One of the main advantages of the presented formalism is that the two main parameters entering the model, magnetic moments μ_i^α and exchange constants J_{ij}, can be calculated from first principles. Thus, our approach in a combination with a density functional theory method provides a parameter-free description of spin waves in substitutional magnetic alloys and ordered materials at finite temperatures.

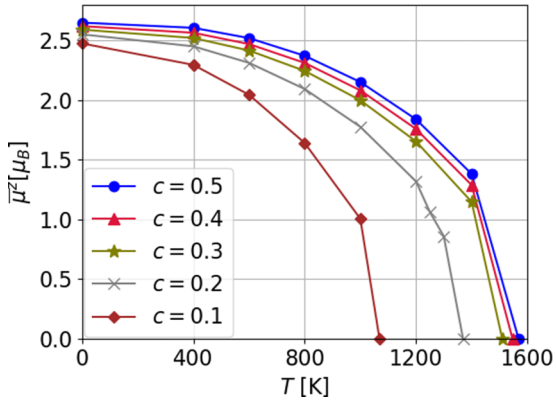

FIG. 3. Thermally averaged magnetic moments' z component of iron in $Fe_{1-c}Co_c$ for different temperatures and cobalt concentrations. Lines are meant as a guide to the eye.

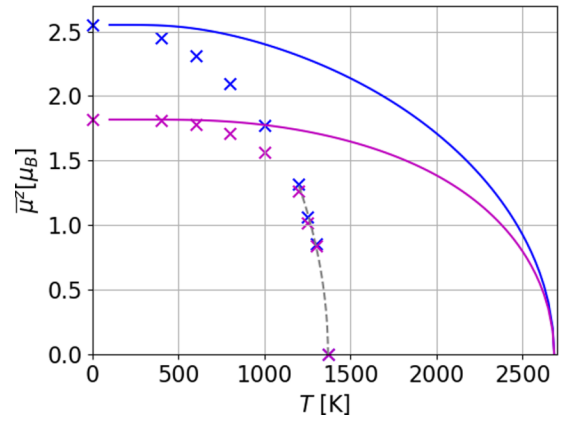

FIG. 4. Thermally averaged magnetic moments' z component in $Fe_{0.8}Co_{0.2}$ for different temperatures within the RPA (crosses) and the MFA (lines). The blue line represents iron while the red line represents cobalt. The dashed line represents the expected behavior of the Heisenberg model near the Curie temperature.

IV. RESULTS

The magnetic moments μ_i^α and exchange parameters J_{ij} of iron-cobalt alloys at various concentrations were evaluated using a first-principles Green's function method within a generalized gradient approximation of density functional theory [51]. The method is designed for bulk materials, surfaces, interfaces, and real-space clusters [52–54]. Disorder effects were taken into account within a coherent potential approximation [55] as it is implemented within multiple scattering theory [56]. The exchange interaction was estimated using the magnetic force theorem formulated for substitutional alloys within the CPA approach [57].

We consider the interaction between 12 shells of neighbors. To ensure the convergence of the calculated properties with the number of neighbor shells, several calculations were performed for up to 30 shells showing practically the same results as with 12.

For better comparability, all the results were calculated using a bcc structure. Furthermore, the interaction parameters J_{ij} are held constant (at their value at $T = 0$ K) while increasing the temperature.

A. Random disorder

1. Curie temperatures

As cobalt has a higher Curie temperature than iron, one would expect a rise of the critical temperature as the concentration of cobalt c is increased. Our results shown in Fig. 3 display this behavior. The points in this figure are the numerical results which were calculated using the methods described in the previous section. Near the magnetic phase transition the characteristic behavior of the averaged magnetic moments is given by

$$\overline{\mu}^z \propto \left(1 - \frac{T}{T_C}\right)^\beta. \tag{31}$$

The critical exponent β has a numeric value of $1/2$ in the case of the Heisenberg model in the RPA [58], which is well known to differ from the experimental value of $\beta \approx 1/3$ [44]. For a system with $c = 0.2$, we used the latter equation as a fitting function with $\beta = 1/2$ for our results close to T_C. It fits very well with our data (cf. Fig. 4). Apart from deploying the RPA, we estimated the Curie temperature using the mean-field approximation (MFA). The MFA is a purely classical model in which the thermally averaged magnetic moments are given by [44]

$$\overline{\mu}^z_{(i)} = \mu \cdot B_{\mu_{(i)}}\left(\frac{g\mu_B B^m_{(i)}\mu_{(i)}}{k_B T}\right), \tag{32}$$

with the Bohr magneton μ_B, the Brillouin function $B_\mu(x)$, and the mean field

$$B^m_{(i)} = \frac{1}{\mu_B \mu_{(i)}} \sum_{\boldsymbol{R}(j)} J_{(i)(j)}(\boldsymbol{R}) c_{(j)} \frac{\overline{\mu}^z_{(j)}}{\mu_{(j)}}. \tag{33}$$

While the RPA is known to underestimate the Curie temperature [40], the MFA overestimates it. This is caused by the fact that the MFA neglects the influence of magnons and therefore only allows spin flips as elementary excitations, which naturally arises at higher energies than magnons [44]. Thus, the combination of these two methods may be used to provide bounds for the approximate theoretical predictions. The MFA equations can be solved iteratively and yield the results shown in Fig. 4 for $Fe_{0.8}Co_{0.2}$. They are almost twice as large as their RPA counterparts, thus providing a rather poor account of the high-temperature behavior of the alloy considered.

The results are summarized in Table I together with experimental results from Refs. [15,16]. While RPA performs fairly well, a clear trend to overestimating the Curie temperature can

TABLE I. Comparison of the Curie temperatures calculated in this work with experimental results in Refs. [15,16].

c	T_C^{RPA} (K)	T_C^{MFA} (K)	T_C (K) in Ref. [16]	T_C (K) in Ref. [15]
0.1	1069	2199	1164	1144
0.2	1369	2684	1225	1211
0.3	1510	2844	1260	1243
0.4	1547	2837	1268	1250
0.5	1568	2803	1265	1243

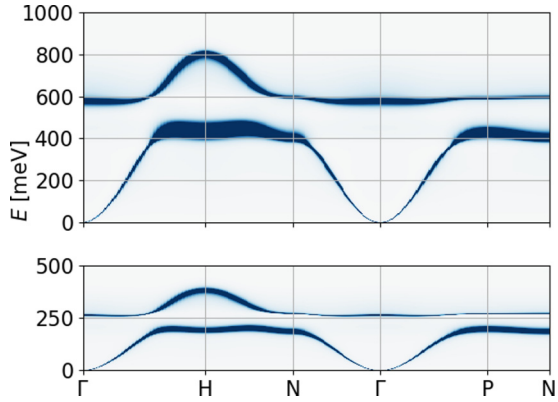

FIG. 5. Magnonic spectrum (trace of the imaginary part of the averaged transverse susceptibility) of $Fe_{0.8}Co_{0.2}$ at $T = 0$ K (top) and $T \approx 0.9T_C$ (bottom).

be seen. Partially, the behavior can be attributed to the fact that in our calculations we restrict the system to a bcc lattice, while the real iron-cobalt system will undergo a structural phase transition at elevated temperatures [16] which is expected to influence the Curie temperature.

2. Magnonic spectrum

We extract the magnonic spectrum from the imaginary part of the retarded averaged susceptibility by calculating its trace $\sum_{(i)} \boldsymbol{\mathcal{X}}_{(i)(i)}(z, \boldsymbol{k})$. The most prominent feature is its band gap appearing due to strongly different interaction strengths and magnetic moments between different constituents. Our results suggest that this band gap is stable up to high temperatures, as can be seen in the result for $Fe_{0.8}Co_{0.2}$ presented in Fig. 5. In the upper (lower) plot the spectrum for the case of $T = 0$ K ($T \approx 0.9T_C$) is shown. Interestingly, the main features of the band structure are preserved as the temperature increases. The scaling (softening) of the magnonic spectrum propositional to the thermally averaged magnetic moment is a feature of the RPA. In this approximation, the magnon energies vanish above the Curie temperature. In a more sophisticated treatment, the spectrum above the critical temperature should feature paramagneticlike excitations emerging as a manifestation of the short-range magnetic order [59].

Let us note that the peaks feature a finite width appearing due to the presence of disorder in the system. The damping is relatively small and increases somewhat only at elevated energies, in particular close to the edges of the band gap. Within the RPA, the width of the peaks is independent of temperature, as can be seen from Eq. (3).

3. Width of the band gap, spin stiffness, and lifetimes

We investigate the spin-wave stiffness constant C describing the quadratic magnon dispersion of the acoustic mode in the long-wavelength limit,

$$E = Ck^2, \tag{34}$$

as well as the size of the band gap. Both decrease roughly proportionally to the average magnetization (see Fig. 6) as the temperature is increased. The reference values at $c = 20\%$ and

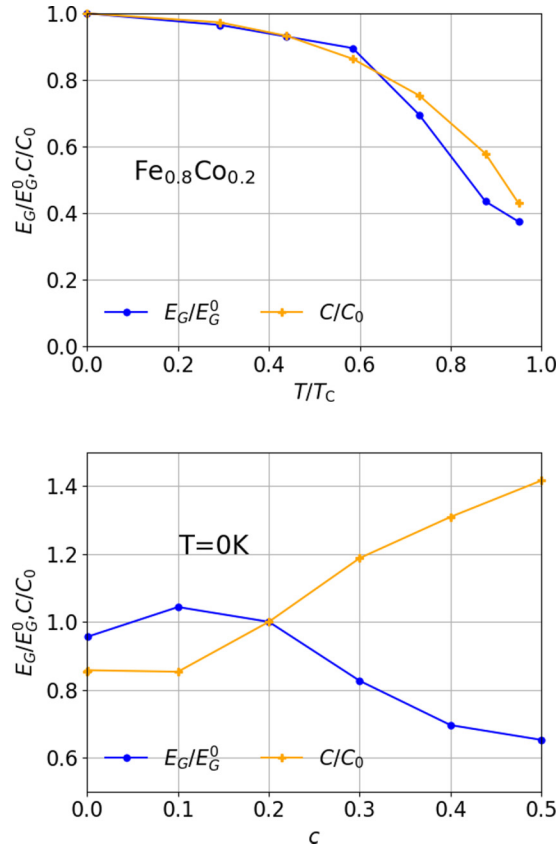

FIG. 6. Relative width of the band gap $\frac{E_G}{E_G^0}$ and relative spin stiffness $\frac{C}{C_0}$ for different cobalt concentrations at $T = 0$ K (bottom) and for different temperatures at $c = 20\%$ (top). All quantities are normalized to their values at $c = 20\%$ and $T = 0$ K ($C_0 \approx 477$ meV Å^2, $E_G^0 = 115$ meV).

$T = 0$ K,

$$C_0 \approx 477 \text{ meV Å}^2, \quad E_G^0 = 115 \text{ meV}, \tag{35}$$

are in reasonable agreement with values from other studies of iron and cobalt [17,60].

Furthermore, we determine the full width at half maximum (FWHM) of the magnon peaks for several wave vectors. The FWHM is computed using a Lorentzian fit function for the imaginary part of the susceptibility as a function of the energy,

$$\operatorname{Im} \chi(E) \approx h \frac{\frac{1}{2}\text{FWHM}}{(E - E_0)^2 + \left(\frac{1}{2}\text{FWHM}\right)^2}, \tag{36}$$

with the location of the maximum E_0 of the peak with scaling factor h. The FWHM is interpreted as the inverse magnon lifetime. In order to facilitate a quantitative comparison, we normalize the width to the energy of the magnon for a particular wave vector. This feature can be interpreted as the inverse of the quality factor, giving the amount of energy leaking from the mode per cycle of the precession.

We recall that in our formalism the finite widths of the magnon resonances arise only due to the action of the disorder. Nevertheless, at constant Co concentration c, the FWHM varies with the temperature as well. In a simple picture, this somewhat unexpected observation can be interpreted as

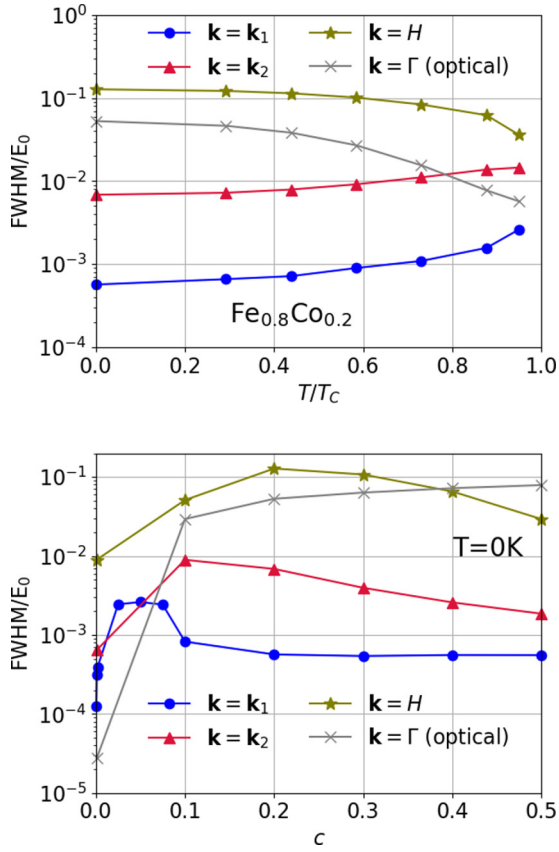

FIG. 7. FWHM at $\boldsymbol{k}_1 = (0.1, 0, 0)\frac{1}{a_B}$, $\boldsymbol{k}_2 = (0.57, 0, 0)\frac{1}{a_B}$ (midway between Γ and H), H and the optical mode at Γ for different cobalt concentrations at $T = 0$ K (bottom), and for different temperatures at $c = 20\%$ (top). The FWHM is normalized by the magnon energy E_0 at the corresponding temperature and concentration.

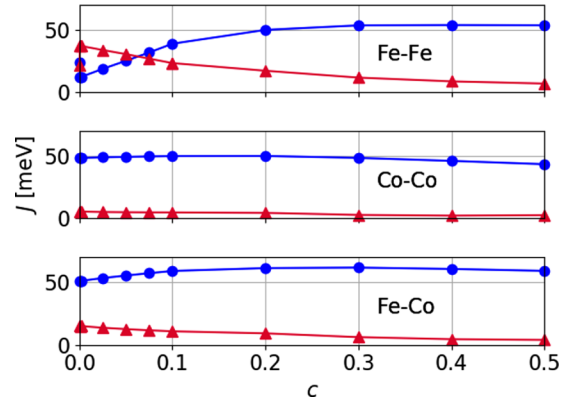

FIG. 8. Exchange interaction in iron-cobalt alloy nearest neighbors (blue circles), and next-nearest neighbors (red triangles). The interaction with atoms in the outer shells is comparably weak.

follows: The scattering rate of magnons of a particular energy on the crystal imperfections (or alternatively the FWHM for weak coupling) is proportional to the concentration of dopants and the density of final magnon states with this energy, as the scattering potential is static. Even though the density of states decreases with temperature, it does not necessarily retain its shape. Thus, for different modes with different wave vectors the density of available finite states will vary as the temperature is raised. As is evident from Fig. 7, this effect depends on the magnon state. With rising temperature, the normalized widths increase for low-energy acoustic magnons, but decrease for magnons at the top of the acoustic branch and in the optical branch.

However, we note again that our prediction concerning the evolution of the width with the temperature, due to the use of the RPA, does not include the main mechanism, i.e., the coupling of the magnons to the thermal bath. In the RPA, without disorder, the magnons would feature an infinite lifetime. In general, it is expected that the thermally induced width should increase with the temperature [61].

The disorder-induced broadening of the magnon peaks in the alloys studied here is found to be in general smaller than 50 meV. Other studies of similar ordered systems which include Landau damping, generally estimate much higher damping. Şaşıoğlu *et al.* [28] study tetragonal FeCo compounds predicting acoustic magnon modes with widths between 50 and 100 meV and optic modes with widths between 60 and 200 meV at the edges of the Brillouin zone based on MBT. Buczek *et al.* [18] predict widths of more than 100 meV for high-energy modes in bulk fcc Co, and more than 60 meV in the case of bulk bcc iron based on TDDFT calculations. They also report spin-wave disappearance in bcc iron close to the H point with widths as high as 550 meV in that region. Consequently, we come to the conclusion that the disorder-induced damping is rather small compared to Landau damping in the considered systems.

The evolution of the magnonic spectrum with the disorder shows several interesting features. For small Co concentrations, the band gap increases slightly and above $c \approx 0.1$ starts to decrease with c (cf. Fig. 6). As mentioned before, in simple terms, the gap arises because of the large difference in the exchange integrals (magnetic interactions) and magnetic moments between different constituents. Figure 8 shows that this difference is pronounced most strongly for low concentrations. The strong increase of the nearest-neighbor Fe-Fe interaction as the Co concentration increases causes the band gap to get narrower, as this exchange integral becomes similar in magnitude to the Co-Co interaction. The enhancement of the Fe-Fe exchange interaction with an increase of Co concentration can be explained by a strong hybridization between the 3d states of Fe and Co atoms. In addition, the presence of Co leads to an enhancement of the density of states at the Fermi level, increasing the Stoner factor and the exchange interaction. An increase of the Co concentration fills up the bands mainly in the minority spin channel. Figure 9 shows the calculated electronic band structure (Bloch spectral function) for $c = 0.5\%$ and $c = 10\%$ for both majority and minority spin channels, respectively. The most important changes for different Co concentrations occur along the Γ-H line for the majority bands and in the vicinity of the Γ point for the minority bands. At low Co concentrations a band along Γ-H is in the Fermi level's vicinity but is not occupied. It is filled up at higher Co concentrations ($c > 5\%$) and leads to a significant increase of the magnetic interaction in the systems. At high cobalt concentrations, it is mainly the difference of the magnetic moments which prevents the closing of the band gap. To

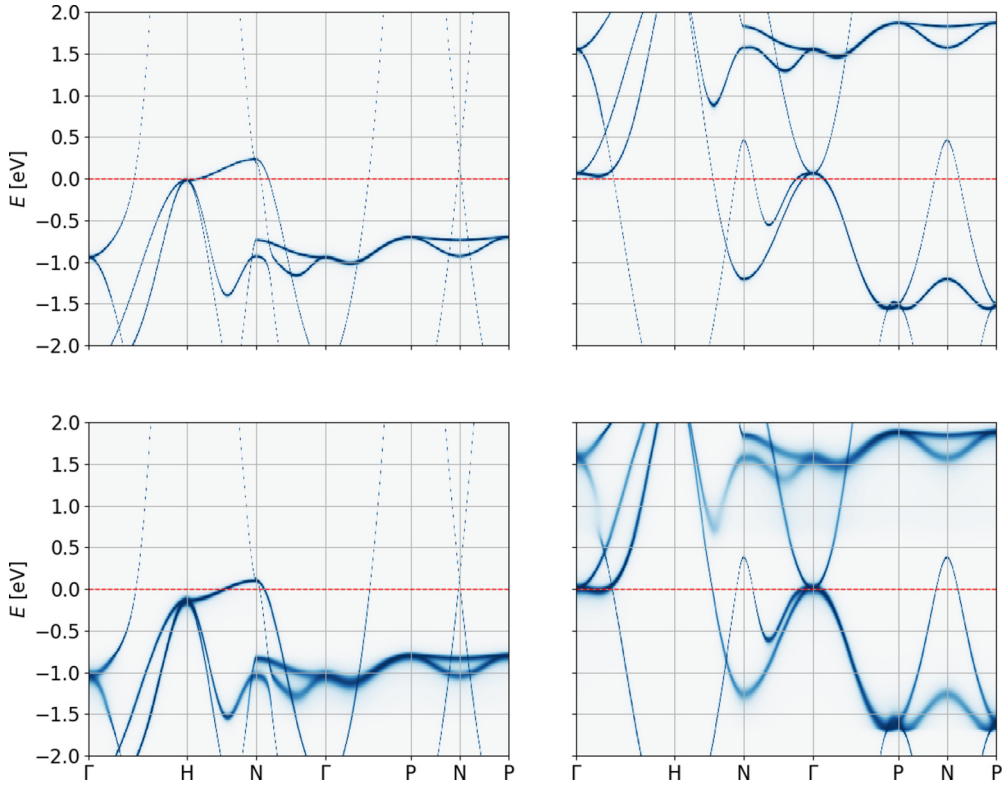

FIG. 9. Bloch spectral functions for $Fe_{0.995}Co_{0.005}$ (upper panels) and $Fe_{0.9}Co_{0.1}$ (lower panels) for majority (left) and minority spin channels, respectively. The red dotted line represents the Fermi energy.

verify this statement we show the spectrum of $Fe_{0.5}Co_{0.5}$ with equal magnetic moments for both constituents $\mu_{Fe} = \mu_{Co}$. As can be seen in Fig. 10, the band gap closes in this case.

Finally, we note that the FWHM shows maxima at certain concentrations, which are caused by the change of the exchange parameters. In Fig. 11, we show the FWHM at $\boldsymbol{k}_1 = (0.1, 0, 0)\frac{1}{a_B}$ and $T = 0$ K for different concentrations compared to the FWHM for the case of fixed interactions.

B. Short-range order

Our theory is formulated in the framework of the single-site CPA, which by definition is not able to account for the appearance of short-range order or any other correlations between the occupation of different sites. However, through our generalization of the theory to lattices with multiple atoms per unit cell, we are able to include short-range order through different occupation probabilities within the unit cell. In this section, we discuss the influence of short-range order using a very simple model. Instead of performing the calculations for the primitive unit cell, we choose for the case of an alloy exhibiting short-range order the usage of a cubic unit cell with

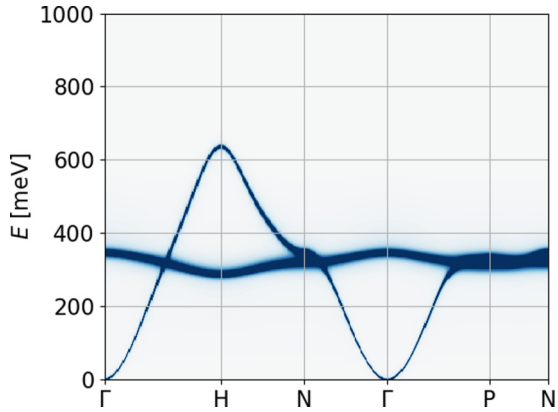

FIG. 10. Magnonic spectrum of $Fe_{0.5}Co_{0.5}$ at $T = 0$ K and $\mu_{Fe} = \mu_{Co}$.

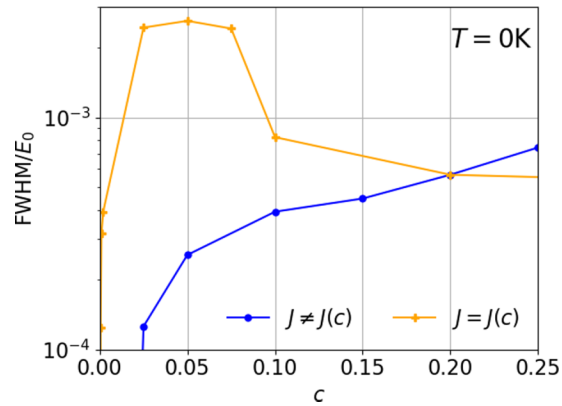

FIG. 11. FWHM$/E_0$ for different concentrations if the interaction parameters are held constant (blue circles) and if they change with the cobalt concentration (orange crosses). The FWHM is normalized by the magnon energy E_0 at $T = 0$ K and the corresponding concentration.

TABLE II. Occupation probabilities for the case of short-range order.

Element	Site 1	Site 2
Fe	1	0.6
Co	0	0.4

two atoms and the occupation probabilities listed in Table II. This configuration corresponds to an alloy in which two cobalt atoms never sit next to each other. The results for the case of random disorder and short-range order are compared in Fig. 12. As there are now two basis sites occupied with two elements according to Table II, the spectrum now consists of three bands. The main result of this test is the verification that the band gap remains present in the case of an alloy exhibiting short-range order.

The magnonic properties discussed above in the alloy with short-range order (SRO) compute to

$$\begin{aligned} E_G &\approx 115\ \text{meV}, \\ \frac{C}{C_0} &= 1.03, \\ \frac{\text{FWHM}}{\text{FWHM}_0} &= 1.92. \end{aligned} \tag{37}$$

It can be seen that the width of the band gap and the spin stiffness hardly change at all, but the FWHM nearly doubles its value. Obviously, this is far from a complete study of the influence of SRO, but it suggests that the inclusion of SRO will only have a minor impact on the width of the band gap.

V. SUMMARY

We presented a first-principles approach to calculate critical magnetic phenomena and spin waves at finite temperatures for complex disordered materials. The method is based on a mapping of a Green's function, obtained within the multiple scattering theory, on the Heisenberg model using a coherent potential approximation. The temperature effects were taken into account within an RPA for the magnonic Green's function.

Our approach is illustrated on disordered iron-cobalt alloys which exhibit many of the properties demanded from magnonic crystals: They exhibit a band gap whose width shows an interesting behavior in the concentration and temperature range studied in this work. The influence of short-range order on the band gap turns out to be of minor importance in our calculations. However, the latter result should only be seen as an intermediate step obtained for one specific type of SRO and needs further investigation.

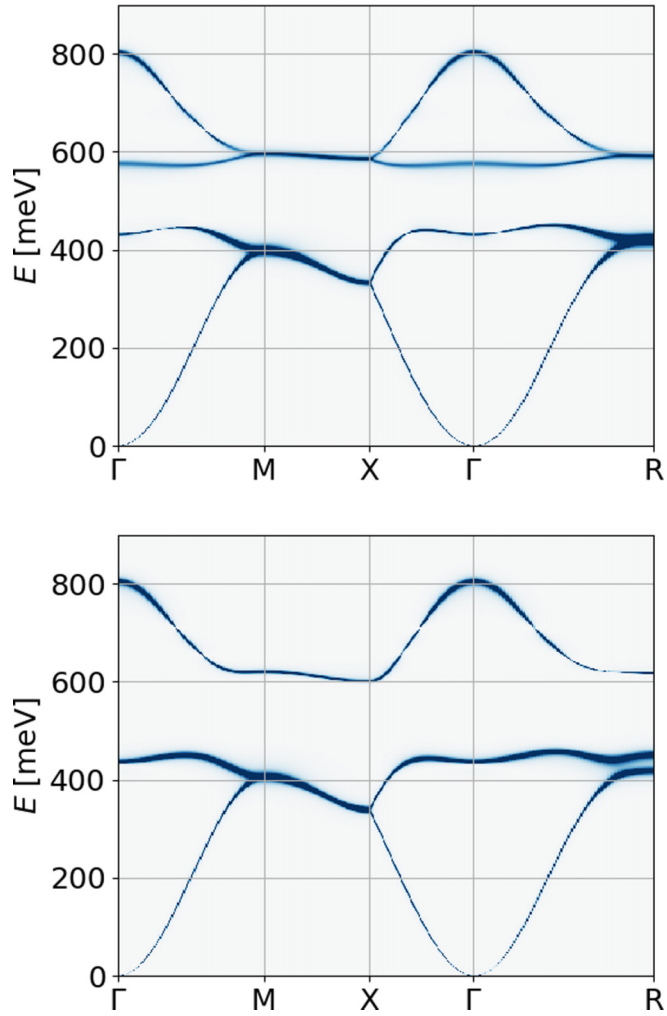

FIG. 12. Magnonic spectrum of $Fe_{0.8}Co_{0.2}$ with random disorder (top), and in a configuration in which all cobalt atoms are isolated from each other according to the occupation probabilities given in Table II at $T = 0$ K (bottom).

The temperature dependence of the bandwidth and the spin stiffness mirrors the decreasing magnetization as the temperature is increased. Thus the treatment of temperature is far from complete. Moreover, the inclusion of Landau damping in the description of disordered systems is a further necessary improvement of the theory which we currently develop.

[1] A. V. Chumak, V. I. Vasyuchka, A. A. Serga, and B. Hillebrands, Nat. Phys. **11**, 453 (2015).
[2] A. Khitun and K. L. Wang, J. Appl. Phys. **110**, 034306 (2011).
[3] H. Al-Wahsh, A. Akjouj, B. Djafari-Rouhani, and L. Dobrzynski, Surf. Sci. Rep. **66**, 29 (2011).
[4] F. Bloch, Z. Phys. **61**, 206 (1930).
[5] A. V. Chumak, A. A. Serga, and B. Hillebrands, J. Phys. D **50**, 244001 (2017).
[6] S. Nikitov, P. Tailhades, and C. Tsai, J. Magn. Magn. Mater. **236**, 320 (2001).
[7] M. Krawczyk and D. Grundler, J. Phys.: Condens. Matter **26**, 123202 (2014).
[8] B. Lenk, H. Ulrichs, F. Garbs, and M. Münzenberg, Phys. Rep. **507**, 107 (2011).
[9] A. V. Sadovnikov, E. N. Beginin, S. A. Odincov, S. E. Sheshukova, Y. P. Sharaevskii, A. I. Stognij, and S. A. Nikitov, Appl. Phys. Lett. **108**, 172411 (2016).

[10] A. V. Sadovnikov, V. A. Gubanov, S. E. Sheshukova, Y. P. Sharaevskii, and S. A. Nikitov, Phys. Rev. Appl. **9**, 051002 (2018).

[11] S. E. Sheshukova, M. A. Morozova, E. N. Beginin, Y. P. Sharaevskii, and S. A. Nikitov, Phys. Wave Phenom. **21**, 304 (2013).

[12] K. Zakeri, Phys. C: Superconductivity **549**, 164 (2018).

[13] P. Buczek, A. Ernst, and L. M. Sandratskii, Phys. Rev. Lett. **105**, 097205 (2010).

[14] P. Buczek, A. Ernst, P. Bruno, and L. M. Sandratskii, Phys. Rev. Lett. **102**, 247206 (2009).

[15] A. S. Normanton, P. E. Bloomfield, F. R. Sale, and B. B. Argent, Met. Sci. **9**, 510 (1975).

[16] T. Nishizawa and K. Ishida, Bull. Alloy Phase Diagrams **5**, 250 (1984).

[17] P. Buczek, A. Ernst, and L. M. Sandratskii, Phys. Rev. Lett. **106**, 157204 (2011).

[18] P. Buczek, A. Ernst, and L. M. Sandratskii, Phys. Rev. B **84**, 174418 (2011).

[19] K. Zakeri, Y. Zhang, T.-H. Chuang, and J. Kirschner, Phys. Rev. Lett. **108**, 197205 (2012).

[20] H. J. Qin, K. Zakeri, A. Ernst, L. M. Sandratskii, P. Buczek, A. Marmodoro, T. H. Chuang, Y. Zhang, and J. Kirschner, Nat. Commun. **6**, 6126 (2015)

[21] P. Buczek, L. M. Sandratskii, N. Buczek, S. Thomas, G. Vignale, and A. Ernst, Phys. Rev. B **94**, 054407 (2016).

[22] P. Buczek, S. Thomas, A. Marmodoro, N. Buczek, X. Zubizarreta, M. Hoffmann, T. Balashov, W. Wulfhekel, K. Zakeri, and A. Ernst, J. Phys.: Condens. Matter **30**, 423001 (2018).

[23] K. Zakeri, Phys. Rep. **545**, 47 (2014).

[24] S. V. Halilov, H. Eschrig, A. Y. Perlov, and P. M. Oppeneer, Phys. Rev. B **58**, 293 (1998).

[25] C. Etz, L. Bergqvist, A. Bergman, A. Taroni, and O. Eriksson, J. Phys.: Condens. Matter **27**, 243202 (2015).

[26] M. Pajda, J. Kudrnovský, I. Turek, V. Drchal, and P. Bruno, Phys. Rev. B **64**, 174402 (2001).

[27] H. B. Callen, Phys. Rev. **130**, 890 (1963).

[28] E. Şaşıoğlu, C. Friedrich, and S. Blügel, Phys. Rev. B **87**, 020410(R) (2013).

[29] H. Okumura, K. Sato, and T. Kotani, Phys. Rev. B **100**, 054419 (2019).

[30] Y. Zhang, P. Buczek, L. Sandratskii, W. X. Tang, J. Prokop, I. Tudosa, T. R. F. Peixoto, K. Zakeri, and J. Kirschner, Phys. Rev. B **81**, 094438 (2010).

[31] M. Etzkorn, P. S. A. Kumar, W. Tang, Y. Zhang, and J. Kirschner, Phys. Rev. B **72**, 184420 (2005).

[32] W. X. Tang, Y. Zhang, I. Tudosa, J. Prokop, M. Etzkorn, and J. Kirschner, Phys. Rev. Lett. **99**, 087202 (2007).

[33] R. Vollmer, M. Etzkorn, P. S. A. Kumar, H. Ibach, and J. Kirschner, Phys. Rev. Lett. **91**, 147201 (2003).

[34] Y. Meng, K. Zakeri, A. Ernst, T.-H. Chuang, H. J. Qin, Y.-J. Chen, and J. Kirschner, Phys. Rev. B **90**, 174437 (2014).

[35] T.-H. Chuang, K. Zakeri, A. Ernst, Y. Zhang, H. J. Qin, Y. Meng, Y.-J. Chen, and J. Kirschner, Phys. Rev. B **89**, 174404 (2014).

[36] K. Zakeri, T.-H. Chuang, A. Ernst, L. M. Sandratskii, P. Buczek, H. J. Qin, Y. Zhang, and J. Kirschner, Nat. Nanotechnol. **8**, 853 (2013).

[37] H. J. Qin, S. Tsurkan, A. Ernst, and K. Zakeri, Phys. Rev. Lett. **123**, 257202 (2019).

[38] K. Zakeri, H. Qin, and A. Ernst, Commun. Phys. **4**, 18 (2021).

[39] H. J. Qin, K. Zakeri, A. Ernst, T.-H. Chuang, Y.-J. Chen, Y. Meng, and J. Kirschner, Phys. Rev. B **88**, 020404(R) (2013).

[40] J. Rusz, I. Turek, and M. Diviš, Phys. Rev. B **71**, 174408 (2005).

[41] J. Rusz, L. Bergqvist, J. Kudrnovsky, and I. Turek, Phys. Rev. B **73**, 214412 (2006).

[42] A. Liechtenstein, M. Katsnelson, V. Antropov, and V. Gubanov, J. Magn. Magn. Mater. **67**, 65 (1987).

[43] I. V. Solovyev, Phys. Rev. B **103**, 104428 (2021).

[44] W. Nolting and A. Ramakanth, *Quantum Theory of Magnetism* (Springer, Berlin, 2009).

[45] F. Yonezawa, Prog. Theor. Phys. **40**, 734 (1968).

[46] T. Matsubara, Prog. Theor. Phys. Suppl. **53**, 202 (1973).

[47] G. X. Tang and W. Nolting, Phys. Rev. B **73**, 024415 (2006).

[48] G. Bouzerar and P. Bruno, Phys. Rev. B **66**, 014410 (2002).

[49] P. E. Blöchl, O. Jepsen, and O. K. Andersen, Phys. Rev. B **49**, 16223 (1994).

[50] S. Geršgorin, Bull. Acad. Sci. URSS, No. 6, 749 (1931).

[51] J. P. Perdew, K. Burke, and M. Ernzerhof, Phys. Rev. Lett. **77**, 3865 (1996).

[52] M. Lüders, A. Ernst, W. M. Temmerman, Z. Szotek, and P. J. Durham, J. Phys.: Condens. Matter **13**, 8587 (2001).

[53] M. Geilhufe, S. Achilles, M. A. Köbis, M. Arnold, I. Mertig, W. Hergert, and A. Ernst, J. Phys.: Condens. Matter **27**, 435202 (2015).

[54] M. Hoffmann, A. Ernst, W. Hergert, V. N. Antonov, W. A. Adeagbo, R. M. Geilhufe, and H. B. Hamed, Phys. Status Solidi B **257**, 1900671 (2020).

[55] P. Soven, Phys. Rev. **156**, 809 (1967).

[56] B. L. Gyorffy, Phys. Rev. B **5**, 2382 (1972).

[57] I. Turek, J. Kudrnovský, V. Drchal, and P. Bruno, Philos. Mag. **86**, 1713 (2006).

[58] E. Kokorina and M. Medvedev, Phys. B: Condens. Matter **416**, 29 (2013).

[59] F. Essenberger, P. Buczek, A. Ernst, L. Sandratskii, and E. K. U. Gross, Phys. Rev. B **86**, 060412(R) (2012).

[60] K. Hüller, J. Magn. Magn. Mater. **61**, 347 (1986).

[61] P. Knoll, C. Thomsen, M. Cardona, and P. Murugaraj, Phys. Rev. B **42**, 4842 (1990).